

Magnetic Nanoemulsions as Candidates for Alzheimer's Disease Dual Imaging Theranostics

¹Orestis Antonoglou,¹Kleoniki Giannousi,^{2,3}Stefanos Mourdikoudis,¹Catherine Dendrinou-Samara*

¹Laboratory of Inorganic Chemistry, Department of Chemistry, Aristotle University of Thessaloniki, Thessaloniki, 54124 Greece.

²Biophysics Group, Department of Physics and Astronomy, University College London, Gower Street, London, WC1E 6BT, UK.

³UCL Healthcare Biomagnetic and Nanomaterials Laboratories, 21 Albemarle Street, London, W1S 4BS, UK.

* Corresponding author, C. Dendrinou-Samara, Email: samkat@chem.auth.gr

Abstract

Alzheimer's disease (AD) is the most prevalent cause of dementia linked to the accumulation of amyloid-beta (A β) plaques-fibrils that impair cognitive functions. Magnetic nanoparticles (MNPs) are emerging as promising tools for the crusade against AD owing to appropriate biocompatibility and facile functionalization that can lead to theranostic agents. Herein, the fabrication of a multimodal (MRI, fluorescence imaging, and drug carrier) magnetic nanoemulsion (MNE) is reported as an AD theranostic candidate. Initially zinc ferrite MNPs of high saturation magnetization (129 emu/g) were synthesized through a modified microwave-assisted polyol process. Memantine (a registered AD drug) was labeled with fluorescein (Mem-Flu) and encapsulated with the MNPs in sodium dodecyl sulfate (SDS) micelles to form the MNE. Small hydrodynamic size (107), high encapsulation (77.5%) and loading efficiencies (86.1%) and sufficient transverse relaxivity (48.7 mM⁻¹s⁻¹) were achieved through the design while sustained release of Mem-Flu was unveiled by in zero-order, first-order, Higuchi and Korsmeyer-Peppas pharmacokinetic models. Moreover, the MNE acquired fluorescence imaging ability of A β ₁₋₄₂ peptide monomers and/or plaques-fibrils via the fluorescein labeling of Memantine. A novel inorganic-organic hybrid multimodal AD theranostic candidate is presented.

1. Introduction

Central nervous system (CNS) disorders remain one of the most dominant challenges faced by modern medicine. ^[1] Amongst them, Alzheimer's disease (AD) is the most prevalent cause of dementia, an irreversible progressive neurodegenerative disease that remains incurable.^[2] Extensive research is carried out on AD aiming to identify all causes and symptoms as well as the major obstacles that the currently utilized drugs face, together with any drawbacks of the current therapeutic strategies. ^[3-5] Thus far, major focus has been set on the amyloid hypothesis referring to the accumulation of toxic amyloid-beta ($A\beta$) plaques-fibrils causing impairment of synaptic and cognitive functions in the brain. ^[6] There are currently four drugs available for AD, donepezil, rivastigmine, galantamine and memantine. ^[7] Memantine is also the only one approved in both Europe and USA. Recent efforts focus on the early diagnosis of AD where milder symptoms are present, combined with a therapeutic strategy with respect to the many causes and symptoms of the disorder. ^[8,9]

Amongst therapeutic candidates for the crusade against AD, magnetic nanoparticles (MNPs) are emerging as promising tools owing to their biocompatibility, theranostic (therapy and diagnosis) capacity and facile functionalization. ^[10, 11] MNPs are protagonists in magnetic resonance imaging (MRI) and magnetic targeting, with various commercial formulations in the industry. ^[12-14] Moreover, secondary nanoarchitectures such as nanocapsules, nanospheres and/or nanoemulsions are proposed for efficient delivery/transfer for CNS disorders like AD ^[15-18], while frameworks such as sodium dodecyl sulfate (SDS), ^[19, 20] polyethylene glycol (PEG) ^[21] and polylactic-co-glycolic acid (PLGA) ^[22] are associated with effective passage through the blood brain barrier (BBB). For example, recently a nanocapsule comprised of Fe_3O_4 MNPs, an anti-transferin monoclonal antibody (OX26) and a PEG/PLGA framework was reported for AD drug delivery. ^[23] However, overbuilt nanoarchitectures suffer from MRI quenching due to the increase of the non-magnetic content while loading efficiency is also not assured. Hence, the prerequisites for such applications are demanding, challenging and several alternatives can be considered, such as dual imaging with an additional method to compensate for MRI quenching.

Herein, expanding our former research on design and biomedical applications of MNPs in therapy and diagnosis, [24-31] we report the fabrication of an AD theranostic magnetic nanoemulsion (MNE) which can function as a MRI, fluorescence imaging, and drug delivery agent. The MNE was designed based on an oil-in-water template using SDS as emulsifier at critical micelle concentration (CMC, 13mg/mL) to reduce overbuilding and MRI quenching. From a biological point of view, ferrites are considered biocompatible as indicated previously by us [69] and other researchers.[64] Also, amongst different ferrites like cobalt, nickel, zinc and manganese, polyol coated zinc ferrite nanoparticles are found highly biocompatible.[64] As magnetic building blocks, zinc doped ferrite MNPs, $Zn_xFe_{3-x}O_4$, were chosen as they represent more stable and advantageous analogues of Fe_3O_4 MNPs. Given that the brain is high in oxygen content (approximately 25% of the total amount of oxygen consumed by the body) oxidation of Fe_3O_4 to the non-magnetic Fe_2O_3 is inevitable whereas the zinc doping will shield the MNPs from the mentioned oxidation. [32] Moreover, appropriate zinc doping ($0.3 < x < 0.4$) can significantly increase the magnetic moment of the MNPs [31, 32]. For the synthesis of the MNPs, a modified microwave-assisted polyol process was employed in a mixed medium of tetraethylene glycol (TEG) and oleylamine (OAm) to achieve tuned zinc doping, small size, high crystallinity and the required hydrophobicity for the secondary nano-architectures.

Memantine has been utilized as an AD drug while labeled with fluorescein (Mem-Flu) via an amide bond formation through EDC-NHS chemistry for fluorescent imaging character. Fluorescein permits the tracking of MNE under visible light excitation. MNPs and Mem-Flu were both encapsulated in SDS to form the MNE. Composition, encapsulation efficiency, loading efficiency, MRI properties, hydrodynamic size and surface charge of the MNE were investigated. The micellar structure of the MNE was examined after fabrication as well as after dilution (ten-fold) to investigate possible changes of the structure in relation to the concentration. Mem-Flu dissolution release profile was estimated in physiological pH and pharmacokinetics analysis was contacted via zero-order, first-order, Higuchi and Korsmeyer-Peppas kinetic models. Fluorescence imaging was carried out on a fluorescence optical microscope after injecting $A\beta_{1-42}$ peptide solutions, either monomers or plaques-fibrils, with the MNE.

2. Methods

2.1. Microwave assisted synthesis of magnetic nanoparticles (MNPs)

A microwave assisted polyol process (MW-PP) was carried out in a MARS 6-240/50-CEM microwave reaction system at a maximum frequency of 2450 MHz and a power of 1800 W. The reaction vessel was a double-walled one consisting of an inner Teflon container liner with temperature and pressure connected sensors and an outer composite sleeve. 1.33 mmol of zinc (II) chloride, $ZnCl_2$, and 2.66 mmol of Iron (III) acetylacetonate, $Fe(acac)_3$, were mixed and dissolved in 20 mL of TEG and 20 mL of OAm, followed by transfer to an autoclave. MW-PP was completed at 260 °C with a ramp time of 14.5 °C/min and a hold time of 30 min and was followed by centrifugation at 5000 rpm, where supernatants were discarded, and a brown-black precipitate was acquired and washed three times with ethanol, for the removal of unreacted precursors.

All the reagents were of analytical grade and were used without any further purification: $Fe(acac)_3$ (Merck, $\geq 99.5\%$, $M = 353.17$ g/mol) $ZnCl_2$ (Merck, $\geq 99.5\%$, $M = 136.315$ g/mol), TEG (Merck, $\geq 99\%$, $M = 222.281$ g/mol) and OA (Merck, $\geq 99\%$, $M = 267.493$ g/mol).

2.2. Fluorescein labeling of Memantine (Mem-Flu) via amide bond formation EDC-NHS chemistry.

0.1 mmol of fluorescein were dissolved into 3 mL of Methanol under magnetic stirring. 3 mL of 2-(N-morpholino)ethanesulfonic acid (MES) buffer (pH = 7-8), containing 0.1 mmol of 1-Ethyl-3-(3-dimethylaminopropyl)carbodiimide (EDC) and 0.15 mmol of N-Hydroxysuccinimide (NHS) were added, followed by the addition of 3 mL of MES buffer containing 0.2 mmol of Memantine. Reaction was carried out for 24 h and the insoluble product (Mem-Flu) was filtered, washed with MES and dried under vacuum.

All the reagents were of analytical grade and were used without any further purification: Fluorescein (BDH, $\geq 95\%$, $M = 332.32$ g/mol), MES (J&K, $\geq 99\%$, $M = 213.25$ g/mol), EDC (TCI, $\geq 98\%$, $M = 191.7$ g/mol), NHS (Sigma, $\geq 98\%$, $M = 115.09$ g/mol), Memantine (3,5-Dimethyl-1-adamantanamine Hydrochloride, J&K, $\geq 99\%$, $M = 215.76$ g/mol).

2.3. Preparation of the magnetic nanoemulsion (MNE).

A stock solution of MNPs was produced by dispersing 5 mg in 15 mL of chloroform. 20 mg of Mem-Flu were dissolved into 5 mL of the stock MNPs' dispersion followed by the addition of 13 mg of sodium dodecyl sulfate (SDS). Finally, 5 mL of ddH₂O were added to start the formation of the emulsion. The emulsion vial was alternating between vortex and sonication apparatuses for 2 h, where in the later the temperature was set at 50 °C. After that, temperature in the sonication apparatus was set at 60 °C to slowly remove all the chloroform.

All the reagents were of analytical grade and were used without any further purification: SDS (Sigma, $\geq 98.5\%$, $M = 288.38$ g/mol).

2.4. Characterization of MNPs, Mem-Flu and MNE.

The elemental composition of the MNPs and the MNE were estimated via inductively coupled plasma atomic emission spectroscopy (ICP-AES) analysis (iCAP 6300, Thermo Scientific).

Crystal structure of the MNPs was investigated through X-ray diffraction (XRD) performed on a Philips PW 1820 diffractometer at a scanning rate of 0.050/3s, in the 2θ range from 20 to 70 °, with Cu K α radiation ($\lambda = 1.5406$ nm).

Magnetic measurements were performed using a vibrating sample magnetometer (VSM) (P.A.R. 155).

Transverse (T_2) relaxation times and nuclear magnetic resonance (¹H-NMR) spectra were collected with an Agilent NMR spectrometer (500 MHz/9 T) equipped with VNMRJ 3.1 software.

Thermogravimetric analysis (TGA) was employed using SETA-RAM SetSys-1200 and carried out in the range from room temperature to 800 °C at a heating rate of 10° C min⁻¹ under an N₂ atmosphere.

Primary particle size and morphology was determined by conventional transmission electron microscopy (TEM) images obtained with JEOL JEM 1200-EX microscope operating at 120 kV. For TEM observations suspensions deposited onto carbon-coated copper grids were used.

The hydrodynamic size and surface charge of the MNE was determined by dynamic light scattering (DLS) and zeta potential measurements, carried out at 25 °C utilizing a Nano ZS Malvern apparatus.

Fourier-transform infrared spectroscopy (FTIR) (2000-1000 cm^{-1}) spectra were recorded using a Nicolet FT-IR 6700 spectrometer with samples prepared as KBr pellets.

Ultra violet/Visible spectroscopy (UV/Vis) spectra were recorded with a Hitachi U-2001 double-beam UV/Vis spectrophotometer.

2.5. Formation and imaging of A β ₁₋₄₂ fibrils

The A β fibrils were formed using a standard procedure previously described. For the aggregation protocol, the peptide was first resuspended in DMSO (5 mM), and then sterile phosphate buffer saline (PBS) was added to bring the peptide to a final concentration of 500 $\mu\text{g}/\text{mL}$. A β peptide amyloidosis was evaluated after agitating and incubating the monomers at 37°C for 24 h. Optical fluorescence microscopy images were obtained using a trinocular EPI fluorescence microscope (HBO illumination system model B-500 TiFL, Optika) equipped with a digital camera set (DIGI, 8 Mpixels) with optical adapter and measuring software. Fluorescence was measured at $\lambda_{\text{ex}} = 475 \text{ nm}$ and $\lambda_{\text{em}} = 535 \text{ nm}$.

Apeptide Beta-Amy 1-42, human (Purity: 95.59%, Shanghai Apeptide Co., Ltd.)

3. Results and Discussion

3.1 Synthetic aspects and preparation of zinc doped ferrite MNPs

A microwave assisted modified polyol process has been applied for the preparation of primary hydrophobic $Zn_xFe_{3-x}O_4$ MNPs in the presence of TEG and OAm. The polyol process is a versatile toolbox that provides control over the 4S's (shape, size, structure, surface chemistry) traits of the as-produced nanoparticles. [33-43] TEG was shown before that can effectively manipulate the composition of the $Zn_xFe_{3-x}O_4$ MNPs to low zinc doping due to the high stability and partial decomposition of Zn-TEG intermediates. [31] It is highly essential to maintain the zinc doping in the $0.3 < x < 0.4$ region as it yields $Zn_xFe_{3-x}O_4$ MNPs with the highest possible saturation magnetization. [32] OAm is included as a stabilizer in the polyol process to provide suitable and more robust coating and colloidal stability. The composition of the as-produced MNPs was estimated by ICP-AES at $Zn_{0.31}Fe_{2.69}O_4$ revealing the desired zinc doping, almost identical to that was previously achieved using solely TEG, and it verifies that OAm did not perturb the doping process. The crystal structure was examined by XRD (Figure 1A). Observed peaks correspond to the spinel crystal structure of zinc ferrite (#22-1012) while no other peaks appear at the diffractograms verifying the purity of the MNPs. Peaks are right shifted due to the zinc doping. [31, 39-41] The crystallite size was calculated from Scherrer formula at 13 nm. Saturation magnetization was found 129 emu/g and it reflects on the appropriate zinc doping (Figure 1B). Additionally, TEM captions were recorded (Figure 1C) and portrayed truncated spherical MNPs with 10.2 ± 0.17 nm sizes (counting over 100 particles), in accordance with the crystallite size. The structure and % w/w proportion of the organic coating were investigated by means of TGA (Figure 2) and FTIR (Figure S1, ESI). FTIR spectrum of MNPs is given in Figure S1 (ESI) where the characteristic polyol peaks (1650 cm^{-1} , C=O bond of the oxidized polyol, 1100 cm^{-1} , C-O-C bond of the polyol backbone) appeared in the spectrum along with peaks for OAm ($1500\text{-}1300\text{ cm}^{-1}$ back bone and C=C bond). In TGA, the observed weight loss is attributed to the decomposition of the organic coating from the surface of MNPs. To investigate structural differentiations, $Zn_{0.30}Fe_{2.7}O_4$ MNPs synthesized solely in TEG [31] were included. It is clear from the TGA curves (Figure 2) that the organic coating is altered when OAm was utilized.

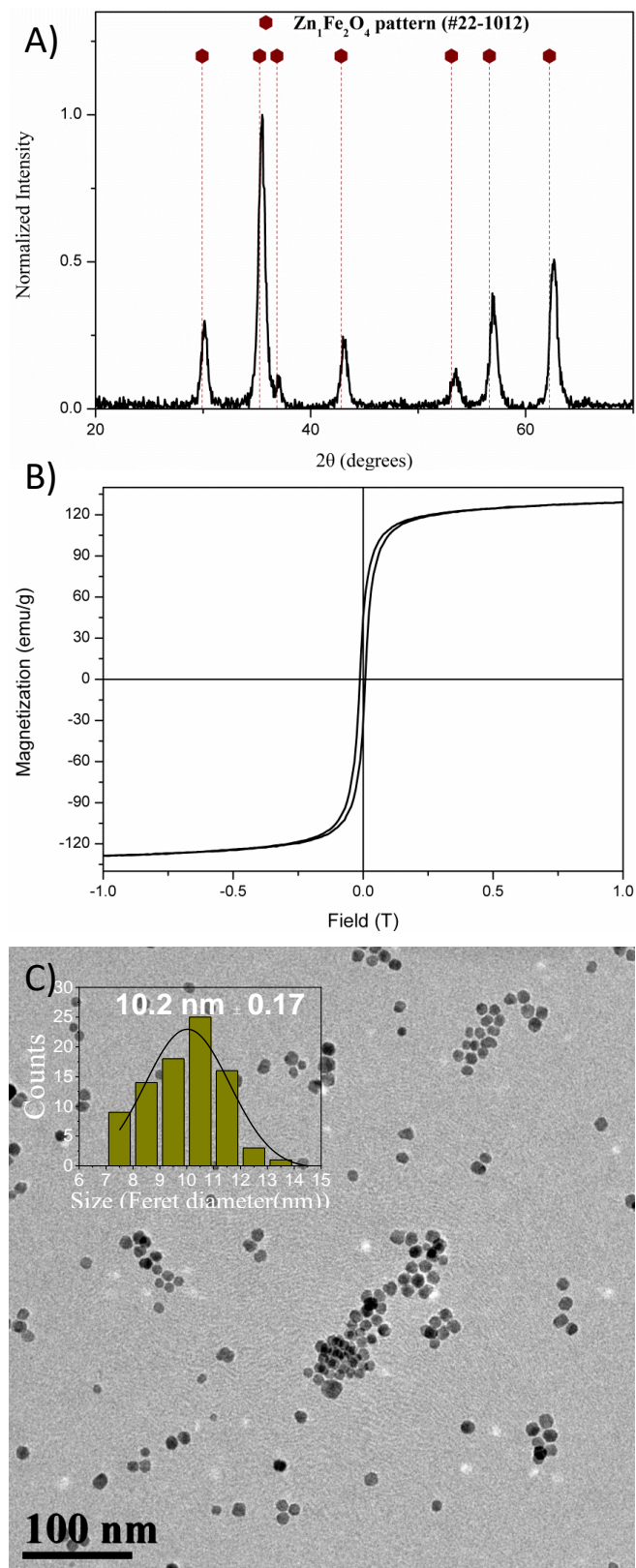


Figure 1. XRD diffractogram (A), VSM hysteresis loop (B) and TEM image (C) of MNPs.

The total weight loss was calculated at 7 and 17% w/w for the $\text{Zn}_{0.3}\text{Fe}_{2.7}\text{O}_4(\text{TEG})$ and $\text{Zn}_{0.31}\text{Fe}_{2.69}\text{O}_4(\text{TEG} + \text{OAm})$ MNPs, respectively. Moreover, in the case of OAm a double layer of coating is observed with a first decomposition step (related to the outer layer) up to 450 °C at 10% w/w and a second decomposition step (inner layer) up to 800 °C at 7% w/w. Interestingly, the second decomposition step (inner layer) is similar to the decomposition of TEG for the $\text{Zn}_{0.3}\text{Fe}_{2.7}\text{O}_4(\text{TEG})$ MNPs. [31] There are previous results on the use of OAm in the polyol process as a stabilizer but no focus was given in the coating arrangement and only the role of OAm was stated. [44-47] Herein, both TEG and OAm remained on the surface of the MNPs with TEG as an inner layer and OAM as an outer one that also provides the hydrophobicity. Hence, the as-produced MNPs of the current work can be better tagged as $\text{Zn}_{0.31}\text{Fe}_{2.69}\text{O}_4@(\text{TEG}(7\% \text{ w/w})@(\text{OAm}(10\% \text{ w/w}))$.

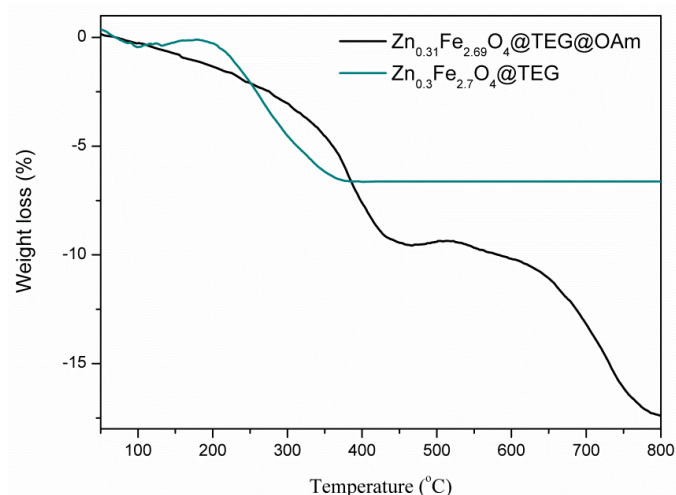


Figure 2. TGA curves of previously published $\text{Zn}_{0.3}\text{Fe}_{2.7}\text{O}_4@(\text{TEG}(7\% \text{ w/w}))$ [31] and $\text{Zn}_{0.31}\text{Fe}_{2.69}\text{O}_4@(\text{TEG}(7\% \text{ w/w})@(\text{OAm}(10\% \text{ w/w}))$ MNPs.

3.2. Fluorescein-labeling of Memantine.

Memantine is a plain organic molecule with very limited characteristic spectroscopic data. Till now, identification and quantification of Memantine has been carried out mainly with chromatographic techniques. The later trend led us and others [48, 49] to conjugate memantine with other compounds that will provide an additional fingerprint to trace. In the current work, Memantine was labeled with fluorescein (Mem-Flu) to gain fluorescent properties and fluorescence imaging traits. This was carried out via EDC/NHS chemistry and amide bond formation between the amine group of

Memantine and the carboxylate group of fluorescein and verified by FTIR, $^1\text{H-NMR}$ and UV-Vis (Figure 3). The characteristic peaks of Amide I ($1700\text{-}1550\text{ cm}^{-1}$), Amide II ($1550\text{-}1450\text{ cm}^{-1}$) and Amide III ($1400\text{-}1200\text{ cm}^{-1}$) were all present in the FTIR spectrum (Figure 3A).^[50] Both Memantine (2.2-0.8 ppm) and fluorescein (8-6.5 ppm) protons appeared in $^1\text{H-NMR}$ spectrum^[51, 52] along with a peak for the amide proton at 8.1 ppm (Figure 3B). In detail, observed peaks are matched to a (0.8 ppm, 6H, Mem), b (1.2 ppm, 2H, Mem), c (1.35 ppm, 4H, Mem), d (1.7 ppm, 4H, Mem), e (1.9 ppm, 2H, Mem), f (2.2 ppm, 1H, Mem), a' (6.5 ppm, 4H, Flu), b' (8 ppm, 1H, Flu), c' (7.8 ppm, 1H, Flu), d' (7.7 ppm, 1H, Flu), e' (7.25 ppm, 1H, Flu) and f' (6.6 ppm, 2H, Flu) protons of the inset of Figure 3B. Spectra were recorded in Methanol- d_4 and solvent peaks were removed from the spectrum. Regarding the optical properties, Memantine has none and in so, the characteristic absorbance of fluorescein was detected shifted from pure fluorescein absorbance (Figure 3C).^[53] The shift is attributed to change of the resonance following to the formation of the amide bond. Based on the above, the labeling was considered effective.

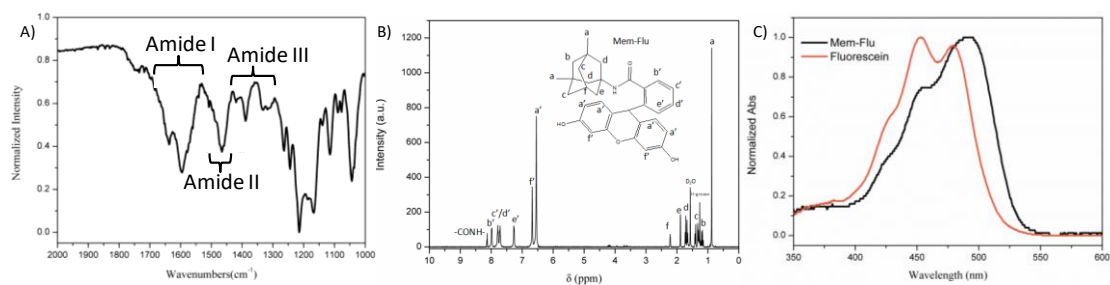


Figure 3. FTIR (A), $^1\text{H-NMR}$ (B) and UV-Vis (C) spectra of Mem-Flu.

3.3. Fabrication of the MNE and encapsulation of MNPs and Mem-Flu

SDS, MNPs and Mem-Flu were employed for the fabrication of the MNE. The lowest amount of SDS required to form micelles (CMC) was utilized (13 mg/mL) in order to provide small micelles and to reduce the non-magnetic component of the MNE and accordingly the MRI contrast quenching. The hydrodynamic size and ζ -potential of MNE were calculated at 107 nm and -38 mV (Figure S2, ESI), respectively, revealing stable nanoemulsion formation. The concentration of encapsulated MNPs was estimated at 0.333 mg/mL by ICP-AES. Reference curves were constructed for Mem-Flu (Figure S3, ESI) and were used for the quantification of the encapsulation. From the total of 20 mg of the starting Mem-Flu, 15.5 mg were effectively encapsulated in

the nanoemulsion for 77.5% encapsulation efficiency and a final concentration of 3.1 mg/mL. Regarding loading efficiency, which translates to the amount of encapsulated Mem-Flu divided by the total amount of SDS + MNPs, it was calculated at 86.1%. These values are very promising as they display reduced overbuilding and the possibility of passive targeting of the brain area via memantine.

The MRI ability of the MNE was investigated by NMR relaxivity measurements (r_2) (Figure 4). Aqueous suspensions in four zinc ferrite concentrations, 0.33, 0.5, 0.67 and 0.83 mM were prepared for the evaluation of T_2 imaging properties. A T_2 imaging agent boosts the relaxation rate according to the equation:

$$R_2 = \frac{1}{T_2} = \left(\frac{1}{T_2}\right)_0 + r_2 C$$

Where R_2 is the relaxation rate, T_2 is the relaxation time, $\left(\frac{1}{T_2}\right)_0$ is the relaxation rate in the absence of the contrast agent, r_2 is the relaxivity and C the concentration (mM). T_2 values given by the NMR apparatus were converted to R_2 values which were plotted vs concentration as seen in Figure 4 and the linear fit provides the slope that is equal to the relaxivity (r_2) (Figure 4 inset). The relaxivity of the MNE was estimated at $48.7 \text{ mM}^{-1} \text{ s}^{-1}$. These measurements suggest a moderate MRI quenching^[31] that is attributed to the SDS framework^[32] but the relaxivity is still sufficient for MRI monitoring^[14].

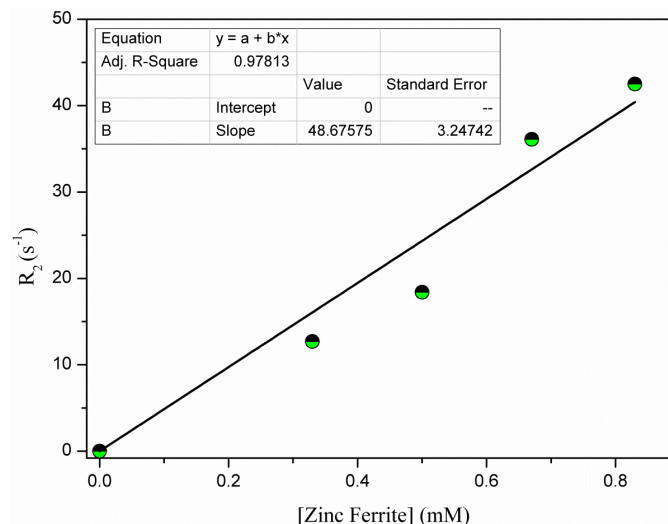


Figure 4. Relaxivity measurements (r_2) for the MNE.

The structure/morphology of the MNE was portrayed via TEM captions given in Figure 5. MNE micelles of $\cong 100 \pm 10$ nm (based on counting of twelve micelles)

can be seen in Figure 5A in accordance with the DLS measurements. Given that SDS was employed in the CMC, dilutions (ten-fold) were carried out to examine changes in the morphology at low concentrations of MNE. TEM captions were recorded after the dilutions and a different arrangement was observed where the diluted MNE adapted a lamellar-like array (Figure 5B). This can be considered a continuous bilayer arrangement where layers of water, which the polar tails of SDS align to, are intervened by layers of encapsulated MNPs and Mem-Flu that the non-polar chains of SDS are trapping. SDS chains can also be spotted in the TEM captions, forming walls between encapsulated MNPs. The lamellar organization of nanoparticles has been reported before for other type of surfactants. [54-56]

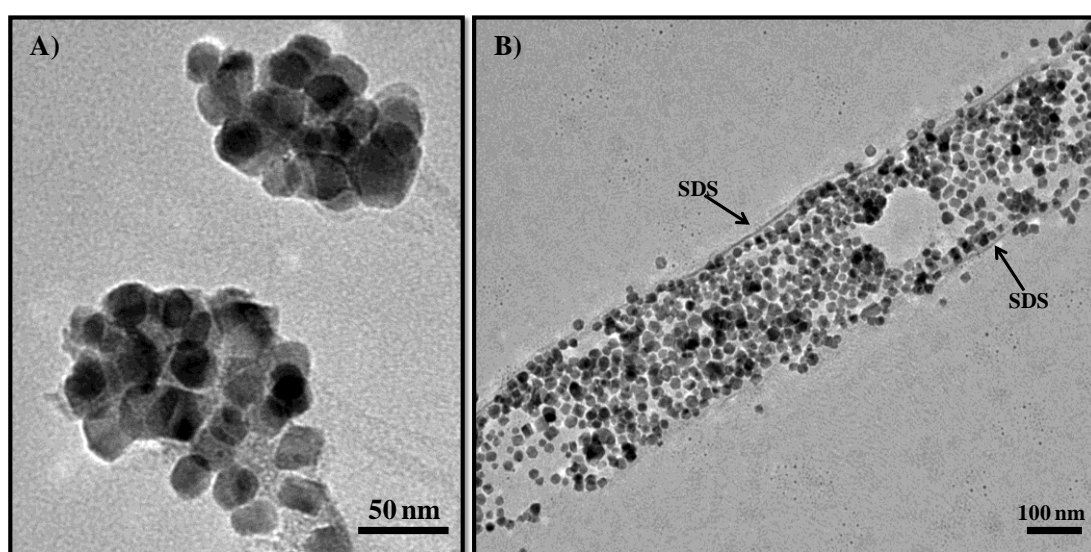


Figure 5. TEM captions of the MNE, revealing micelles of $\cong 100 \pm 10$ nm (A) and a lamellar-like arrangement after ten-fold dilutions (B).

SDS framework presents an ideal biocompatible coating for BBB crossing as indicated before from other studies. [19, 20, 66] Organic coatings are used to cover MNPs to deceive the reticulo-endothelial system and/or the formation of a dense protein corona, since “naked” ferrites following intravenous administration, either are readily recognized by serum proteins, opsonins and immune cells resulting in opsonization and/or phagocytosis, or deleted by reticuloendothelial system (RES) of liver and spleen.. D. Lachowicz, *et al.* showed that polysaccharide coated zinc ferrite nanoparticles of 10 nm core size with a hydrodynamic size of 200 nm, parameters that are in line to the presented magnetic nanoemulsions, are nontoxic in concentrations up to 0.54 mg/mL in murine neuroblastoma cells.[67] In another study, polyol coated (Diethylene glycol,

DEG) ZnFe_2O_4 MNPs of small core size (10 nm) were found of enhanced biocompatibility up to 1 mg mL^{-1} concentration in adenocarcinoma lung cancer cell line A549, compared to other ferrites such as cobalt, nickel and manganese.^[64]

3.4 Mem-Flu release profile

The essential element of a drug carrying nanoplatform is sustained release of the active components. The profile of Mem-Flu released from the MNE was estimated via the dialysis bag approach using the Mem-Flu reference curves (Figure S3, ESI). Moreover, it was compared with the free Memantine release profile derived with the same method by Sánchez-López *et al.* ^[49] but with HPLC since Memantine has no optical response. Results can be viewed in the Figure 6 and values are summarized on Table 1. Aliquots were removed in time intervals of 0.5, 1, 1.5, 2, 3, 4, 5, 6 and 24 hours. Release was conducted at physiological pH (7.2). Free Memantine is released over 50% in the first hour whereas this happened after 3 hours for the MNE encapsulated Mem-Flu, verifying the sustained release. Total release of free Memantine took place after 4 hours while MNE encapsulated Mem-Flu was released at 67% on that time period and reached $\cong 100\%$ release after 24 hours (97%).

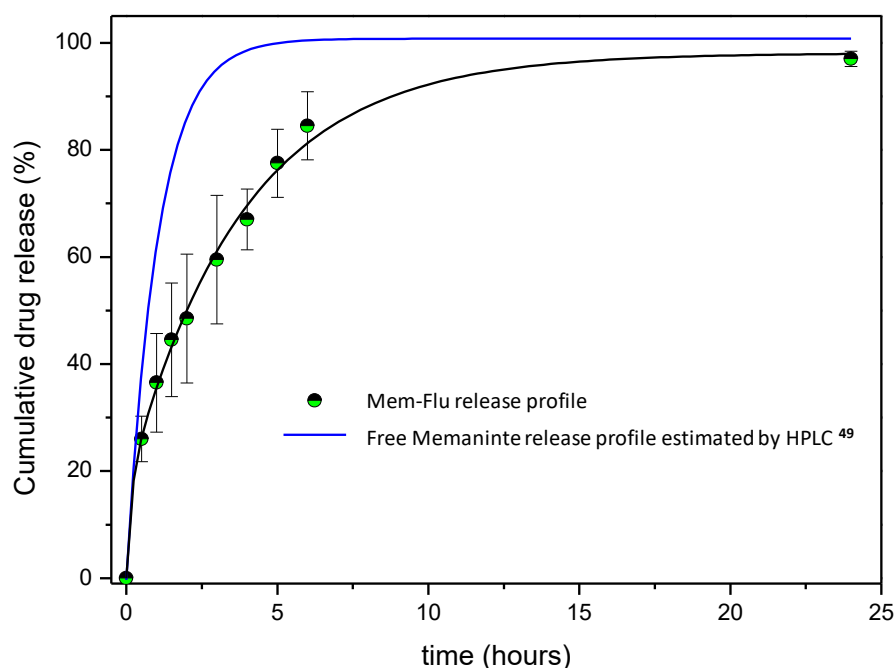


Figure 6. MNE encapsulated Mem-Flu and free Memantine (estimated by Sánchez-López *et al.* via HPLC ^[49]) release profiles.

Pharmacokinetics study was conducted to analyze the release mechanism. Data were fitted to zero order, first order, Higuchi and Korsmeyer-Peppas models and the linearity of the models detailed the aptness of each one. [57, 58] Results can be viewed in the Figure 7 and values are summarized on Table 2. Figure 7A depicts the zero order model regarding a release profile independent of remaining concentration. This is obviously not the case here with a fitting value of $R^2 = 0.89$. The concentration dependent first order kinetics are illustrated in Figure 7B, derived after transforming the release data into logarithmic. The fitting value was provided at $R^2 = 0.98$ and verified a concentration dependent release profile. Data were then converted to fit the Higuchi model (Figure 7C) where high R^2 and slope (K_H) values are correlated to a diffusion release mechanism. Herein, R^2 and K_H values were calculated at 0.99 and 33.82, respectively, and confirmed the diffusion mechanism of the release. The Korsmeyer-Peppas model was employed to categorize the diffusion mechanism (Figure 7D). In this model, both release and time are converted to logarithmic and the slope (N value) classifies the diffusion amongst Fickian ($N < 0.5$), non-Fickian anomalous transport ($0.5 < N < 1$) and polymer swelling ($N > 1$). Accordingly, the N value was estimated at 0.47, revealing a normal Fickian diffusion release of Mem-Flu from the MNE.

Table 1. MNE encapsulated Mem-Flu release over time (%).

Time (hours)	MNE Encapsulated Mem-Flu release (%)
0.5	26
1	37
1.5	45
2	49
3	60
4	67
5	78
6	85
24	97

3.5. Fluorescence imaging of amyloid-beta (A β) monomers and plaques-fibrils

Fluorescein is an excellent fluorescent probe for imaging of biomolecules [39, 59] and could be also an ideal A β probe for *in vivo* detection of amyloids in brain tissue, under the prerequisite of having high binding affinity with the peptide. [60] While the fabricated MNE possess MRI characteristics that enable *in vivo* monitoring, Mem-Flu will enable effective imaging of the state of the A β peptide, whether in its monomer or plaque-fibril form. Additionally, the fluorescence imaging can compensate for the moderate MRI quenching of the SDS framework. Currently, it is supported that the amyloid plaques are nonpathogenic, since are insoluble deposits of A β peptides. On the contrary, the soluble oligomers of the peptides are very toxic. [61] Thus, it is very important to find a way to detect all the states of A β peptides.

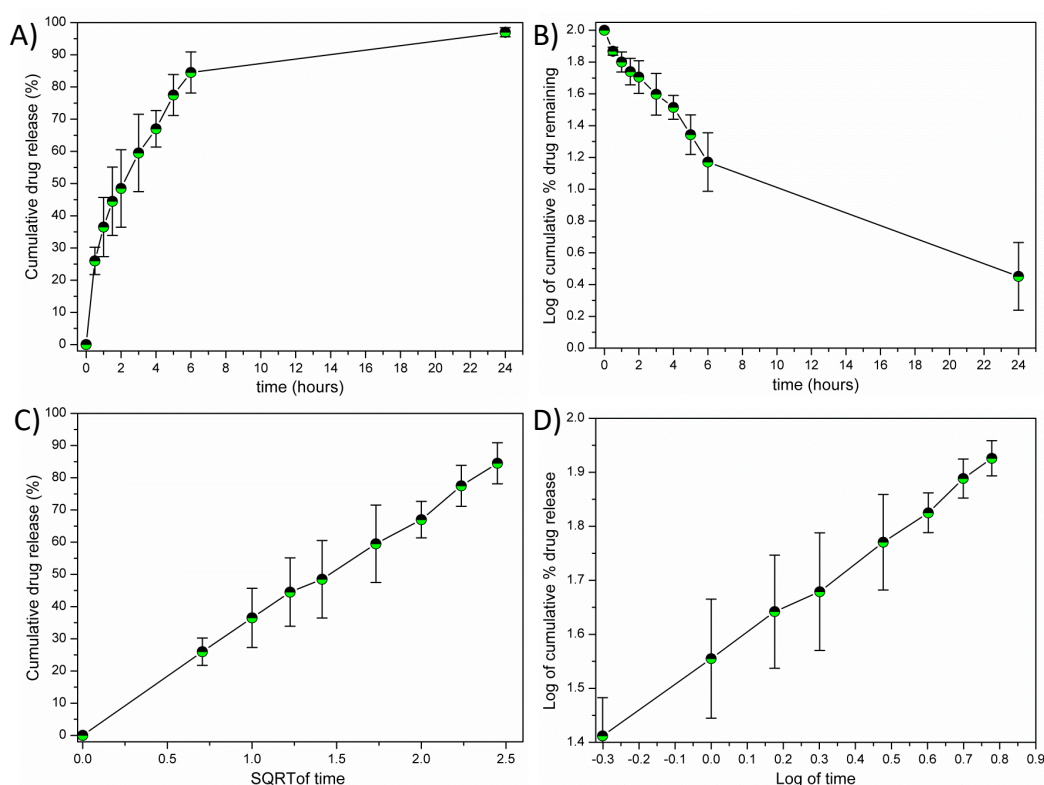


Figure 7. Pharmacokinetics conducted to analyze the release mechanism of MNE encapsulated Mem-Flu via zero order (A), first order (B), Higuchi (C) and Korsmeier-Peppas models (D).

Table 2. Pharmacokinetic values for MNE encapsulated Mem-Flu derived from zero order, first order, Higuchi and Korsmeier-Peppas models.

Zero order	First order	Higuchi		Korsmeyer Peppas	
R ²	R ²	R ²	K _H	R ²	N
0.889	0.98	0.997	33.82	0.997	0.47

For that purpose, A β ₁₋₄₂ peptide solutions were studied both in the monomeric and plaque-fibril configuration and were injected with different concentrations of MNE (1 and 100 μ g/mL), containing the Mem-Flu. Captions can be seen in Figure 8 where both the A β monomers (Figure 8A,B) and the plaques-fibrils (Figure 8C,D) were effectively portrayed and distinguished in a concentration dependent manner. The concentrations tested were both low, highlighting the high selectivity of Mem-Flu for A β . Plaques-fibrils appeared as large asymmetrical aggregates of monomers, as captioned elsewhere.^[62] Moreover, the emission wavelength is compatible with brain imaging (> 450 nm), as it minimizes the background fluorescence from brain tissue.^[63]

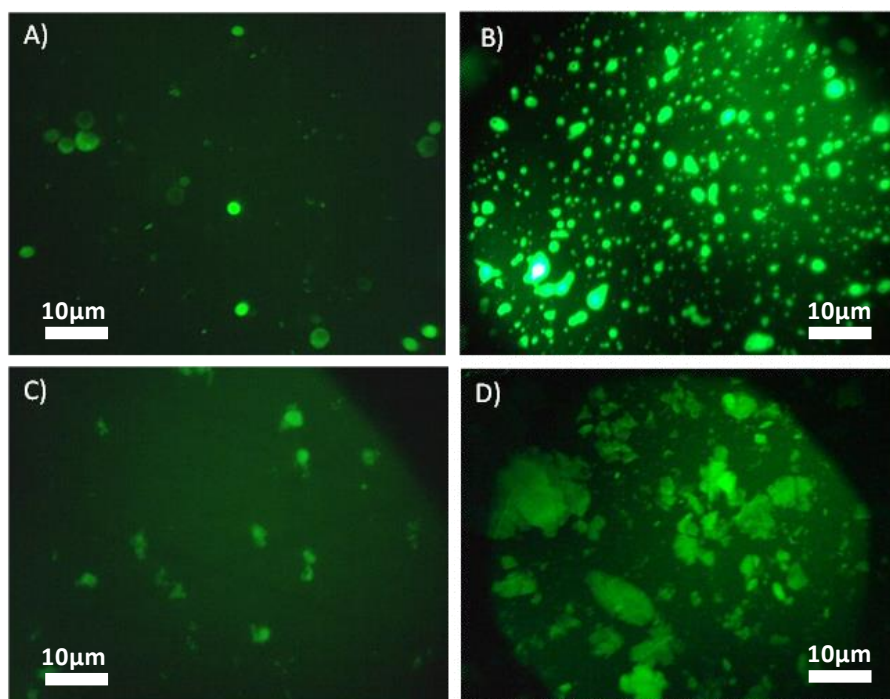


Figure 8. Fluorescence imaging (fluorescence optical microscope) of A β ₁₋₄₂ monomers (A,B) and plaques (C,D) after injecting 1 μ g/mL MNE (A,C) and 100 μ g/mL (B,D) into the A β peptide solutions. Fluorescence was measured at $\lambda_{\text{ex}} = 475$ nm and $\lambda_{\text{em}} = 535$ nm.

Concerning the size of the MNE, it seems to be big enough to avoid renal clearance and small enough for reaching the brain from blood circulation.^[65] However, the exact sizing criterion for optimal BBB transport is still somewhat disputed.^[68]

4. Conclusions

CNS disorders pose a serious threat to human life and health. The asymptomatic nature of AD in the early stages and the limitations in current clinical diagnostic methods make the early diagnosis and treatment of AD difficult. The area of dual imaging theranostic magnetic nanomaterials can effectively help to resolve present inadequacies. However, overbuilding of nanoarchitectures needs to be avoided for high theranostic efficiency. In the present work, the fabrication of an AD theranostic MNE with MRI, fluorescence imaging, and drug delivery characteristics has been developed. A low amount of SDS (CMC) was utilized to avoid intense MRI quenching and a sufficient relaxivity was achieved for the MNE, $48.7 \text{ mM}^{-1}\text{s}^{-1}$. Moreover, to compensate for the moderate MRI quenching, a Memantine-fluorescein conjugate (Mem-Flu) was successfully encapsulated in the MNE with high encapsulation and loading efficiencies, 77.5 and 86.1%, respectively. In that manner, apart from MRI monitoring, the MNE acquired fluorescence imaging ability of A β peptide monomers and/or plaques-fibrils that proved an image-guided intervention. Moreover, high memantine loading enables the possibility of passive targeting of the brain area. Changes in the morphology of the MNE were recorded after ten-fold dilutions, as nanomicelles were converted to a lamellar-like arrangement. This highlights that dilution of MNEs can promote structural differentiation with possible diverse functionalities and is something to consider in bioapplications. All these findings formulate a very promising CNS theranostic candidate for AD early diagnosis and intervention. Given our previous results that also gave spark to the potential of zinc ferrite MNPs in protein anti-fibrillation,^[31] AD *in vivo* experiments are under investigation. Considering *in vivo* studies and the BBB challenge as our future prospect, we have currently initiated some preliminary theoretical models for nose to brain passage of the developed magnetic nanoemulsions via the use of external magnets

Conflict of interest

The authors declare that there are no conflicts of interest.

Acknowledgements

This project «Functionalized Magnetic Nanoparticles candidates for Alzheimer's disease» is implemented through /has been co-financed by the Operational Program "Human Resources Development, Education and Lifelong Learning" and is co-financed by the European Union (European Social Fund) and Greek national funds.

Author Contributions

CD-S: conceptualization and supervision. OA, KG, SM: methodology. OA, KG, SM, CD-S: validation. OA, KG: formal analysis and writing—original draft preparation. OA, KG, SM: investigation. CD-S, SM: resources. OA, KG: data curation. CD-S, SM: writing—review and editing. CD-S: project administration and funding acquisition.

5. References

- [1] A.S. Kesselheim, T.J. Hwang, J.M. Franklin. *Nat. Rev. Drug Discov.*, 2015, **14**, 815.
- [2] M. P. Mattson. *Nature*, 2004, **430**, 631.
- [3] A. s. Association. *Alzheimer's & Dementia*, 2017, **12**, 459.
- [4] M. Citron. *Nat. Rev. Drug Discovery*, 2010, **9**, 387.

- [5] R. Jakob-Roetne, H. Jacobsen. *Angew. Chem., Int. Ed.*, 2009, **48**, 3030.
- [6] X. Han, G. He. *ACS Chem. Neurosci.*, 2018, **9**, 198.
- [7] W. M. Pardridge. *Drug Discov. Today*, 2007, **12**, 54.
- [8] M.G. Savelieff, G. Nam, J. Kang, H. J. Lee, M. Lee, M. H. Lim. *Chem. Rev.*, 2019, **119**, 1221.
- [9] X.-Y. Jiang, T.-K. Chen, J.-T. Zhou, S.-Y. He, H.-Y. Yang, Y. Chen, W. Qu, F. Feng, H.-P. Sun. *ACS Med. Chem. Lett.*, 2018, **9**, 171.
- [10] D. Azria, S. Blanquer, J. M. Verdier, E. Belamie. *J. Mater. Chem. B*, 2017, **5**, 7216.
- [11] H. Derakhshankhah, S. Sajadimajd, S. Jafari, Z. Izadi, S. Sarvari, M. Sharifi, M. Falahati, F. Moakedi, W.C. Akeyo Muganda, M. Muller, M. Raoudi, J.F. Presley, *Nanomedicine*, 2020, **24**, 102149.
- [12] S. Mornet, S. Vasseur, F. Grasset, E. Duguet. *J. Mater. Chem.*, 2004, **14**, 2161.
- [13] H. B. Na, I. C. Song, T. Hyeon, *Adv. Mater.*, 2009, **21**, 2133.
- [14] N. V. S. Vallabani, S. Singh. *3 Biotech.*, 2018, **8**, 279.
- [15] H. L. Wong, X. Y. Wu, R. Bendayan. *Adv. Drug Deliv. Rev.*, 2012, **64**, 686.
- [16] S. Soni, R. K. Ruhela, B. Medhi. *Adv. Pharm. Bull.*, 2016, **6**, 319.
- [17] C. Saraiva, C. Praça, R. Ferreira, T. Santos, L. Ferreira, L. Bernardino. *J. Control. Release*, 2016, **235**, 34.
- [18] L. Wu, J. Zhang, W. Watanabe. *Adv. Drug Deliv. Rev.*, 2011, **63**, 456.
- [19] G. Wang, J.-J. Wang, F. Li, S.-S. Tony To. *J. Pharm. Sci.*, 2016, **105**, 1535.
- [20] H.M. Shubar, S. Lachenmaier, M. M. Heimesaat, U. Lohman, R. Mauludin, R. H. Mueller, R. Fitzner, K. Borner, O. Liesenfeld. *J. Drug Target.*, 2011, **19**, 114.
- [21] S. Ku, F. Yan, Y. Wang, Y. Sun, N. Yang, L. Ye. *Biochem. Biophys. Res. Commun.*, 2010, **394**, 871.
- [22] S. Gelperina, O. Maksimenko, A. Khalansky, L. Vanchugova, E. Shipulo, K. Abbasova, R. Berdiev, S. Wohlfart, N. Chepurnova, J. Kreuter. *Eur. J. Pharm. Biopharm.*, 2010, **74**, 157.
- [23] N. Cui, H. Lu, M. Li. *J. Biomed. Nanotechnol.*, 2018, **14**, 1017.
- [24] K. Vamvakidis, M. Katsikini, D. Sakellari, E.C. Paloura, O. Kalogirou, C. Dendrinou-Samara. *Dalton Trans.*, 2014, **43**, 12754.
- [25] M. Menelaou, K. Georgoula, K. Simeonidis, C. Dendrinou-Samara. *Dalton Trans.*, 2014, **43**, 3626.
- [26] M. Menelaou, Z. Iatridi, I. Tsougos, K. Vasiou, C. Dendrinou-Samara, G. Bokias. *Dalton Trans.*, 2015, **44**, 10980.

- [27] V. Georgiadou, G. Makris, D. Papagiannopoulou, G. Vourlias, C. Dendrinou-Samara. *ACS Appl. Mater. Interfaces*, 2016, **8**, 9345.
- [28] Z. Iatridi, K. Vamvakidis, I. Tsougos, K. Vassiou, C. Dendrinou-Samara, G. Bokias. *ACS Appl. Mater. Interfaces*, 2016, **8**, 35059.
- [29] K. Vamvakidis, S. Mourdikoudis, A. Makridis, E. Paulidou, M. Angelakeris, C. Dendrinou-Samara. *J. Colloid Interface Sci.*, 2018, **511**, 101.
- [30] K. Giannousi, E. Koutroumpis, V. Georgiadou, V. Karagkounis, C. Dendrinou-Samara. *Eur. J. Inorg. Chem.*, 2019, **14**, 1895.
- [31] K. Giannousi, O. Antonoglou, C. Dendrinou-Samara. *ACS Chem. Neurosci.*, 2019, **8**, 3796.
- [32] N. Lee, T. Hyeon. *Chem. Soc. Rev.*, 2012, **41**, 2575.
- [33] H. Dong, Y.C. Chen, C. Feldmann. *Green Chem.*, 2015, **17**, 4107.
- [34] F. Fiévet, S. Ammar-Merah, R. Brayner, F. Chau, M. Giraud, F. Mammeri, J. Peron, J.Y. Piquemal, L. Sicard, G. Viau, *Chem. Soc. Rev.*, 2018, **47**, 5187.
- [35] D. Larcher, R. Patrice. *J. Solid State Chem.*, 2000, **154**, 405.
- [36] A. J. Biacchi, R. E. Schaak. *ACS Nano*, 2011, **5**, 8089.
- [37] H. Dong, M. Roming, C. Feldmann. *Part. Part. Syst. Character.*, 2015, **32**, 467.
- [38] K. J. Carroll, J. Ulises Reveles, M. D. Shultz, S. N. Khanna, E. E. Carpenter. *J. Phys. Chem. C*, 2011, **115**, 2656.
- [39] O. Antonoglou, K. Giannousi, J. Arvanitidis, S. Mourdikoudis, A. Pantazaki, C. Dendrinou-Samara. *J. Inorg. Biochem.*, 2017, **177**, 159.
- [40] O. Antonoglou, J. Moustaka, I.-D. S. Adamakis, I. Sperdouli, A. A. Pantazaki, M. Moustakas, C. Dendrinou-Samara. *ACS Appl. Mater. Interfaces*, 2018, **10**, 4450.
- [41] O. Antonoglou, E. Founta, V. Karagkounis, E. Pavlidou, G. Litsardakis, S. Mourdikoudis, N. T. K. Thanh, C. Dendrinou-Samara. *Front. Chem.*, 2019, **7**, 817.
- [42] P. Tryfon, O. Antonoglou, G. Vourlias, S. Mourdikoudis, O. Menkisoglou, C. Dendrinou-Samara. *ACS Appl. Nano Mater.*, 2019, **6**, 3870.
- [43] K. Vamvakidis, M. Katsikini, G. Vourlias, M. Angelakeris, C. E. Paloura, C. Dendrinou-Samara. *Dalton Trans.* 2015, **44**, 5396.
- [44] S. Mourdikoudis, L. M. Liz-Marzán. *Chem. Mater.*, 2013, **9**, 1465.
- [45] E. Hammarberg, C. Feldmann. *Z. Anorg. Allg. Chem.*, 2013, **639**, 887.
- [46] S. Güner, A. Baykal, Md. Amir, H. Güngüneş, M. Geleri, H. Sözeri, S. E. Shirsath, M. Sertkol. *J. Alloys Compd.*, 2016, **688**, 675.

- [47] D. Kodama, K. Shinoda, R. Kasuya, K. Tohji, M. Doi, J. Balachandran. *J. Appl. Phys.*, 2010, **107**, 320.
- [48] S. Laserra, A. Basit, P. Sozio, L. Marinelli, E. Fornasari, I. Cacciatore, M. Ciulla, H. Türkez, F. Geyikoglu, A. Di Stefano. *Int. J. Pharm.*, 2015, **485**, 183.
- [49] E. Sánchez-López, M. Ettcheto, M. A. Egea, M. Espina, A. Cano, A. C. Calpena, A. Camins, N. Carmona, A. M. Silva, E. B. Souto, M. L. García. *J. Nanobiotechnol.*, 2018, **32**, 1.
- [50] F. Mallamace, C. Corsaro, D. Mallamace, S. Vasi, C. Vasi, G. Dugo. *Comput. Struct. Biotechnol. J.*, 2015, **13**, 33.
- [51] F. Trotta, F. Caldera, R. Cavalli, A. Mele, C. Punta, L. Melone, F. Castiglione, B. Rossi, M. Ferro, V. Crupi, D. Majolino, V. Venuti, D. Scalarone. *Beilstein. J. Org. Chem.*, 2014, **10**, 2586.
- [52] A. Sahu, M. Narayanam, M. Kurmi, M. K. Ladumor, S. Singh. *Magn. Reson. Chem.*, 2016, **54**, 632.
- [53] P. Siejak, D. Frackowiak. *J. Phys. Chem. B*, 2005, **30**, 14382.
- [54] S. G. Jang, A. Khan, C. J. Hawker, E. J. Kramer. *Macromolecules*, 2012, **45**, 1553.
- [55] V. T. A. Nguyen, M. Gauthier, O. Sandre. *Nanomaterials*, 2014, **6**, 628.
- [56] M. S. Bakshi, P. Sharma, T. S. Banipal, G. Kaur, K. Torigoe, N. O. Petersen, F. Possmayer. *J. Nanosci. Nanotechnol.*, 2007, **7**, 916.
- [57] R. Gouda, H. Baishya, Z. Qing. *J. Develop. Drugs.*, 2017, **6**, 1.
- [58] H. K. Shaikh, R. V. Kshirsagar, S. G. Patil. *World J. Pharm. Res.*, 2015, **4**, 324.
- [59] K. Giannousi, M. Menelaou, J. Arvanitidis, M. Angelakeris, A. Pantazaki, C. Dendrinou-Samara. *J. Mater. Chem. B*, 2015, **3**, 5341.
- [60] M. Zhou, X. Wang, Z. Liu, L. Yu, S. Hu, L. Chen, W. Zheng. *Curr. Alzheimer Res.*, 2014, **11**, 221.
- [61] T. Yang, S. Li, H. Xu, D. M. Walsh, D. J. Selkoe. *J. Neurosci.*, 2017, **37**, 152.
- [62] S. C. Lee, H. H. Park, S. H. Kim, S. H. Koh, S. H. Han, M. Y. Yoon. *Anal. Chem.*, 2019, **91**, 5573.
- [63] W. M. Chang, M. Dakanali, C. C. Capule, C. J. Sigurdson, J. Yang, E. A. Theodorakis. *ACS Chem. Neurosci.*, 2011, **2**, 249.
- [64] S. Sabale, V. Jadhav, V. Khot, X. Zhu, M. Xin, H. Chen. *J Mater Sci: Mater Med*, 2015, 26, 127.
- [65] M. A. Hady, O. M. Saved, M. A. Akl, *Colloids Surf B Biointerfaces*, 2020, **193**, 111076.

- [66] A. Saija, P. Princi, D. Trombetta, M. Lanza, A. De Pasquale. *Exp. Brain Res.*, 1997, **115**, 546-551.
- [67] D. Lachowicz, W. Gorka, A. Kmita, A. Benasik, J. Zukriwski, W. Szczerba, M. Sikora, C. Kapusta, S. Zapotoczny. *J. Mater. Chem. B*, 2019, **7**, 2962-2973.
- [68] D. Furtado *et al.* *Adv. Mater.* 2018, **30**, 1801362.
- [69] V. Georgiadou *et al.* *Dalton Trans.*, 2014, **43**, 6377.